Physics Letters B 844 (2023) 138092

Contents lists available at ScienceDirect

Physics Letters B

journal homepage: www.elsevier.com/locate/physletb

Sensitivity of the *r*-process rare-earth peak abundances to nuclear masses

Y.W. Hao (郝艺伟)[a,b], Y.F. Niu (牛一斐)[a,b,*], Z.M. Niu (牛中明)[c]

[a] School of Nuclear Science and Technology, Lanzhou University, Lanzhou 730000, People's Republic of China
[b] Frontiers Science Center for Rare isotopes, Lanzhou University, Lanzhou 730000, People's Republic of China
[c] School of Physics and Optoelectronic Engineering, Anhui University, Hefei 230601, People's Republic of China

ARTICLE INFO

Article history:
Received 1 February 2023
Received in revised form 8 July 2023
Accepted 17 July 2023
Available online 24 July 2023
Editor: B. Balantekin

Keywords:
Nucleosynthesis
R-process
Rare-Earth peak
Nuclear mass

ABSTRACT

The sensitivity of the *r*-process rare-earth peak abundances to nuclear masses has been studied in different astrophysical scenarios. The most impactful nuclei lie along the *r*-process paths at *r*-process freeze-out and at the time when the neutron-capture timescale is approximately 3 times of the β-decay timescale ($\tau_{n\gamma} \approx 3\tau_{\beta}$), corresponding to the onset and completion of rare-earth peak formation, respectively. In astrophysical scenario with fission involved, the sensitivities for nuclei lying along the *r*-process path at freeze-out are masked by the large contribution of fission products to the rare-earth peak abundances. This work provides recommended targets for future researches and thus helps to increase the understanding of rare-earth peak formation mechanism and the efficacy of the rare-earth peak as an *r*-process site diagnostic.

1. Introduction

The rapid neutron-capture process (*r*-process) of stellar nucleosynthesis explains the origin of about half of the elements heavier than iron in the universe [1]. The astrophysical sites of the *r*-process are still one of the most intriguing open problems, and have not been identified yet. There are a number of candidate sites have been proposed, neutrino-driven wind (NDW) of core-collapse supernovae (CCSNe) [2,3], magnetohydrodynamically driven jet (MHDJ) from rapidly rotating and strongly magnetized CCSNe [4], neutron star mergers (NSMs) [5,6] and so on, as described in details in Refs. [7,8]. It is undoubted that more than one astrophysical site has contributed to the observed solar system *r*-process abundances [9–11]. However, there is still no consensus on the dominant site for *r*-process nucleosynthesis. In addition to the uncertainty of astrophysical site, the large deviations among different theoretical predictions of the properties of neutron-rich nuclei far from the stability also introduce a significant source of uncertainty in *r*-process nucleosynthesis simulations [12–16].

Despite these difficulties, many prominent features in the *r*-process abundance distribution have been learned after more than a half century of study and observational progress. Two most prominent features of the *r*-process abundance in the solar system are $A = 130$ and $A = 195$ peaks, which are attributed to closed neutron shells occurring at magic neutron numbers 82 and 126 [1,17]. In addition to the two main peaks, another important feature is the rare-earth peak at $A \sim 165$. However, the production mechanism of the rare-earth peak is still a controversial topic. In contrast to the second and third *r*-process peaks, which result from a combination of long β-decay half-lives and other nuclear properties at closed shells, the rare-earth peak lies away from closed neutron shells, so its formation must occur by a different mechanism.

At present, three distinct mechanisms have been proposed to explain the rare-earth peak formation. The first one is the dynamical formation mechanism in hot *r*-process scenario proposed by Surman et al. [18]. The peak formation requires the presence of a nuclear physics feature such as a deformation maximum or a subshell closure in the rare-earth region, which can present itself as a "kink" in the neutron separation energy contours in this region [19]. The peak formation occurs as the *r*-process path encounters the region with the kink during the decay back to stability. Subsequently, Mumpower et al. [20] came up with another dynamical mechanism for cold *r*-process scenario where $(n, \lambda) \rightleftarrows (\lambda, n)$ equilibrium fails early. The peak formation will occur if the *r*-process path encounters a special structure in the neutron capture rate contours involving slow neutron capture rates in this region. Recently, more experimental [19,21–24] and theoretical works [25–27] have been carried out based on the hypothesis of the dynamical formation mechanism. The third mechanism is

* Corresponding author.
E-mail address: niuyf@lzu.edu.cnY.F. Niu (牛一斐).

https://doi.org/10.1016/j.physletb.2023.138092

fission, which is hypothesized that this peak is formed by the deposition of fission fragments if the distribution of fission fragments is favorable [28,29]. We cannot deny it as a possible solution that the rare-earth peak is formed by a combination of the dynamical mechanism and fission mechanism. In this paper, by comparing the *r*-process simulations in different astrophysical conditions and based on different fission fragment distribution models, we offer new insights into the correlation between the dynamical mechanism and the fission mechanism of the rare-earth peak formation.

In principle, the rare-earth peak can be used to constrain astrophysical conditions when comparing simulations to the solar *r*-process abundances [30]. However, the height and location of the rare-earth peak are extremely sensitive not only to astrophysical conditions at late times in the *r*-process but also to nuclear physics inputs [18,30,31]. Due to the large uncertainties of nuclear features of neutron-rich nuclei, the variance bands of the abundance distributions are larger than the peak itself, and it is hard to distinguish the abundance patterns produced by different astrophysical environments [13,32–34]. Thus, to develop the capacity of using the rare-earth peak to constrain the *r*-process site, the reductions of uncertainties of nuclear physics inputs are required.

Since the experimental measurements of nuclear features of neutron-rich nuclei are difficult, sensitivity studies to address the roles of individual nuclear data in *r*-process simulations are necessary, which can identify the key nuclei that have strong impact on the *r*-process abundances [13]. So far, *r*-process sensitivity studies have been performed for nuclear masses [32–36], neutron-capture rates [37–40], and β-decay rates [40,41]. Nuclear masses are arguably the most important input for the *r*-process, because they determine the reaction energies and go into the calculations of all involved reaction rates. These sensitivity studies of *r*-process abundances to nuclear masses obtained a universal and robust conclusion: the nuclei with the most impactful masses lie along the equilibrium *r*-process paths and the decay paths of closed shell nuclei [32,33,36]. However, these studies focus more on global effects on the abundance distributions caused by mass variations. Important nuclei for the study of rare-earth peak are still not clear. Therefore, in this paper, we will perform sensitivity studies focused on the rare-earth peak formation by varying every single nuclear mass of nuclei in the region of interest for the peak formation proposed in Ref. [20]. We aim to identify the most influential nuclei and in return show their effects on the rare-earth peak abundance pattern. The most influential nuclei are recommended to be the targets of future researches and thus help to increase the understanding of rare-earth peak formation mechanism and the efficacy of the rare-earth peak as an *r*-process site diagnostic.

2. *r*-process calculations

We use the nuclear network NucNet [42] to simulate *r*-process nucleosynthesis, which consists of more than 6000 isotopes, including neutrons, protons, and heavy isotopes with $Z \leq 102$. We take nuclear masses from the finite-range droplet model (FRDM) [43], and the neutron-capture rates are calculated with the publicly available statistical model code TALYS [44] with the same nuclear masses for *r*-process calculation as inputs. The β-decay rates are taken from JINA REACLIB database [45]. Fission is included as in Ref. [46]. We perform *r*-process calculations using a parameterized trajectory as implemented in Refs. [20,30], where the density as a function of time is given by:

$$\rho(t) = \rho_1 \exp(-t/\tau) + \rho_2 \left(\frac{\Delta}{\Delta + t}\right)^n \quad (1)$$

where $\rho_1 + \rho_2$ is the density at time t = 0, and Δ is a constant real number. The early-time behavior of the outflow is dominated by the first term on the right-hand side while the late-time behavior is dominated by the second term. The temperature is determined from the density and entropy, and the initial composition is determined by the choice of electron fraction Y_e [47,48]. The parameter n sets the thermodynamic behavior of the evolution at the late-time of *r*-process. A hot *r*-process evolution has typical values of $n \sim 2$, which is characteristic of wind models [47,49]. Values of $n \geq 5$ are typical of cold *r*-process evolutions and correspond to a faster decline of density and temperature [30,50]. Due to the uncertainty of astrophysical site for the *r*-process, the nucleosynthesis in different astrophysical conditions is investigated by changing the parameters Y_e, τ, and entropy rather than specific sites. For this work, we chose three distinct astrophysical scenarios. The first is a classic hot *r*-process with entropy 150 k_B, an initial electron fraction of Y_e = 0.3, a timescale of τ = 20 ms, and freeze-out power law of $n = 2$. The second trajectory is also a hot *r*-process with entropy 233 k_B, Y_e = 0.1, τ = 35 ms, and $n = 2$. The third trajectory is a cold *r*-process with entropy 150 k_B, Y_e = 0.2, τ = 20 ms, and $n = 6$. The high entropy conditions are possible in neutrino-driven wind environments, however we employ lower electron fractions than typically found in detailed supernova models [51] without exotic physics, as implemented in [13,20,21,25,26,30,46,52]. In all scenarios, we start nucleosynthesis calculations at initial temperature T = 10 GK. We label these three trajectories as trajectories *hot1*, *hot2*, and *cold*, respectively. In *hot1* scenario, the nucleosynthesis process do not significantly populate fissioning nuclei due to fewer neutrons in the environment and fission can be negligible. However, in *hot2* and *cold* scenarios, a large number of fissioning nuclei can be produced and plenty of fission fragments are deposited at around $A = 110 \sim 170$ region based on the GEF fission fragment distribution model [53], which predict fission yields in the neutron-rich regions contain both a symmetric and asymmetric component [46,54]. So in these cases fission will affect the rare-earth peak formation. In order to explore the scenario with fission but without contributions from fission fragments to the rare-earth peak formation, we ran an additional set of simulations in the *cold* scenario, where we use a simple symmetric split for the fission product distributions. This ensures that fission fragments fall in the $A \sim 130$ peak region and do not directly influence the rare-earth peak formation. We label this set of simulations as trajectory *cold-sym* in the following.

For each trajectory chosen, the mass sensitivity study begins with a baseline simulation which defines the choice of inputs from nuclear models. Subsequent simulations are then performed with these fixed inputs, but allowing nuclear mass of a certain nucleus to vary. Currently, the rms deviations between theoretical mass models and the available experimental data are around 0.5 MeV. However, for neutron-rich nuclei far away from the experimental known region, the differences between the nuclear masses predicted by different mass models can exceed several MeV [13,26,32,36]. In this work, we consider mass variations of ± 1 MeV as in Refs. [32,36]. When a certain nuclear mass is varied, we recalculate the neutron-capture rates of all involved nuclei that depend on the changed mass. We realize that β-decay rates also should be calculated consistently with the changed mass, however, such calculations have not been performed so far. We plan to explore the sensitivity of *r*-process nucleosynthesis to β-decay rates in future work. So all the β-decay rates remain unchanged during our mass variations. Each time nuclear mass is changed, a corresponding final abundance pattern is produced. We repeated this step for 414 nuclei, which cover the region of interest for the formation of the rare-earth peak as summarized in Ref. [20]. Finally, we compare the final rare-earth peak abundance patterns produced with the nuclear mass variations to the baseline pattern using the sensitivity measure F,

$$F = 100 \sum_{A=150}^{178} \frac{|\,Y_{+1}(A) - Y_{origin}(A)\,| + |\,Y_{-1}(A) - Y_{origin}(A)\,|}{Y_{origin}(A)}. \tag{2}$$

$Y_{origin}(A)$ is the final baseline abundance, and $Y_{+1}(A)$ and $Y_{-1}(A)$ are final abundances of the simulations where a single nuclear mass is increased or decreased by 1 MeV, respectively. The F metric quantifies the impact of the mass on the abundance pattern in the rare-earth peak region through the summation over mass numbers of $A = 150 - 178$.

3. Results and discussions

To illustrate the evolution of the formation of the rare-earth peak, we depict in Fig. 1 the time evolution of abundances summed over isobaric chains in three mass regions of the left side of the rare-earth peak elements (REE-Left) $A = 150 - 159$, the middle of rare-earth peak elements (REE-Middle) $A = 160 - 170$, and the right side of rare-earth peak elements (REE-Right) $A = 171 - 178$. The first vertical line mark the time at r-process freeze-out which is defined as the neutron-to-seed ratio $R = 1$. The second vertical line indicates the point that the timescale of neutron capture $\tau_{n\gamma}$ is approximately 3 times of the β-decay timescale τ_β. The timescales of neutron capture and β decay are defined as

$$\frac{1}{\tau_{n\gamma}} = \frac{\sum_{Z,A} N_n \langle \sigma v \rangle_{(Z,A)} Y(Z,A)}{\sum_{Z,A} Y(Z,A)},$$
$$\frac{1}{\tau_\beta} = \frac{\sum_{Z,A} \lambda_\beta(Z,A) Y(Z,A)}{\sum_{Z,A} Y(Z,A)}, \tag{3}$$

respectively, where N_n is the neutron number density, $\langle \sigma v \rangle_{(Z,A)}$ is the neutron-capture rate, $\lambda_\beta(Z,A)$ is the β-decay rate, and $Y(Z,A)$ is the abundance of nucleus (Z, A). From Fig. 1 we find that the rare-earth peak starts to form at freeze-out, and is completely formed at the point of $\tau_{n\gamma} \approx 3\tau_\beta$ in all cases considered here except *cold-sym*, which can be seen clearly in Fig. 2.

In the case of *hot1*, there are fewer neutrons in the environment, so the freeze-out ($R = 1$) occurs earlier than other cases, and the dynamic evolution of the r-process is very fast. The three summed abundances rise sharply when neutron-to-seed ratio $R > 1$, and change slowly later after $R = 1$. An increase of the abundance in the mass region $A = 160 - 170$ occurs after freeze-out, while the abundances of mass region $A = 150 - 159$ and $A = 171 - 178$ decrease, which results in a peak formation around $A \sim 165$. After freeze-out, the total abundance of rare-earth peak ($A = 150 - 178$) is roughly a constant due to the missing contribution of fission fragments since fission can be negligible in this environment.

In the *hot2*, *cold*, and *cold-sym* cases, the abundance in the rare-earth peak region increases at first, and then actually starts to shrink as material moves to higher mass number. But just after the third r-process peak and heavier nuclei are produced, it grows again. After freeze-out, the abundance in the mass region $A = 160 - 170$ becomes the largest, corresponding to the onset of peak formation. Since a large number of fission products are deposited at rare-earth peak region in the cases of *hot2* and *cold* scenarios, the abundance in total rare-earth mass region ($A = 150 - 178$) is rising continuously after freeze-out until the rare-earth peak is formed. In contrast, in the cases of *hot1* and *cold-sym*, the total abundance in rare-earth region is roughly constant. In addition, in the *cold-sym* case where we use the simple symmetric fission treatment, fission fragments don't contribute to the rare-earth region, and the material in the rare-earth peak region moves to higher mass number due to the late-time neutron

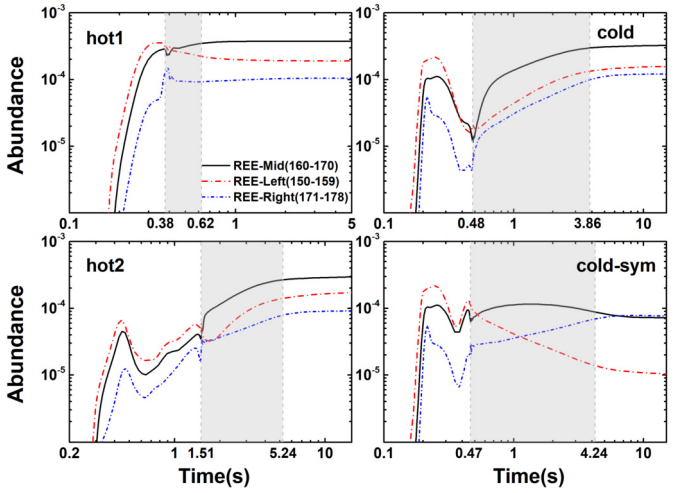

Fig. 1. Time evolution of abundances summed over isobaric chains in the three mass regions $A = 150 - 159$ (red), $A = 160 - 170$ (black), and $A = 171 - 178$ (blue) in four different scenarios. The shaded area represents the time interval of rare-earth peak formation, from the time of r-process freeze-out ($R = 1$) to the point where the timescale of neutron capture is approximately 3 times of the timescale of β decay ($\tau_{n\gamma} \approx 3\tau_\beta$).

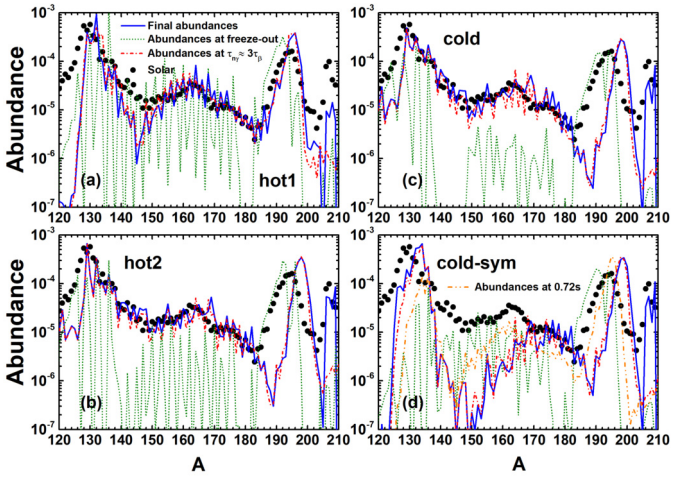

Fig. 2. The abundance distributions in *hot1*, *hot2*, *cold*, and *cold-sym* scenarios. The blue solid line represents the final r-process abundances at a simulation time of 1 Gyr, and the green dotted line and red dashed line correspond to the abundance patterns at r-process freeze-out and at the point of $\tau_{n\gamma} \approx 3\tau_\beta$, respectively. In the *cold-sym* scenario, the orange dashed line represents the abundance pattern at the time of 0.72 s. The dots represent the solar r-process abundance pattern [55].

capture effect after freeze-out [56,57]. So the material in mass region $A = 150 - 159$ and $A = 160 - 170$ is shifted to $A = 171 - 178$, which corresponds to a wrong peak position as shown in Fig. 2.

The final abundance distributions at a simulation time of 1 Gyr and the abundance patterns at r-process freeze-out and at the point of $\tau_{n\gamma} \approx 3\tau_\beta$ in *hot1*, *hot2*, *cold*, and *cold-sym* scenarios are shown in Fig. 2. It can be clearly seen that the rare-earth peak has been formed at the point of $\tau_{n\gamma} \approx 3\tau_\beta$, where the rare-earth peak abundances are roughly consistent with the final abundances. In *hot1* scenario, the basic features of the r-process abundance are reproduced, but the abundances around the valley after the second r-process peak are underestimated. In *hot2* and *cold* scenarios, the final abundances are both roughly consistent with the solar r-process abundances except a slight shift of the rare-earth peak and the third r-process peak position to higher mass number, and the underestimated abundances around the valley after the second r-process peak are improved by the contribution of fission fragments. However, in *cold-sym* scenario, the rare-earth peak cannot

be reproduced correctly, indicating the unreasonable distribution of fission fragments.

In the case of *hot1* without fission, the rare-earth peak is formed by dynamical mechanism [20] which depends on the local nuclear properties in the region between the *r*-process paths at 0.38 s (onset time) and 0.62 s (completion time of rare-earth peak formation), as shown in Fig. 3. In the case of *cold-sym* with symmetric fission fragments distribution, a bump similar to the shape of rare-earth peak is also formed at 0.72 s due to the dynamical mechanism as shown in panel (d) of Fig. 2. But over time, the material in rare-earth mass region moves to higher mass number due to the late-time neutron capture effect, and the solar rare-earth peak abundances cannot be reproduced. The wrong position of the peak may be due to the improper nuclear physics inputs such as nuclear masses, β-decay rates and neutron-capture rates, which is also responsible to the slight shift of the rare-earth peak and the third *r*-process peak position to higher mass number for *cold* and *hot2* scenarios with the reasonable fission fragment distributions. However, if we use the fission fragment distribution calculated by GEF model as in the *cold* case, fission products are deposited at rare-earth peak region and play a role in shaping rare-earth peak abundances, leading to the agreement with the solar *r*-process abundance pattern. So we can conclude that in the astrophysical scenario where a large number of fissioning nuclei can be produced, the rare-earth peak abundances are largely set by the fission deposition, and a successful formation of rare-earth peak requires reasonable fission fragment distributions. In addition, as shown in Fig. 3 the strong sensitivity of the rare-earth peak abundances to nuclear masses on the *r*-process path indicates that the dynamical mechanism also plays an important role.

Fig. 3 shows the results of the mass sensitivity studies for *hot1*, *hot2*, *cold*, and *cold-sym* scenarios, and the 30 most impactful nuclei are listed in Table 1 in the appendix. As a general result, we find influential nuclear masses are mainly distributed in two regions: the first one lies between 15 and 20 neutrons away from stability which we defined as region I; the second one lies between 7 and 15 neutrons away from stability which is defined as region II.

In region I, the nuclei with high sensitivity measures F lie along the *r*-process path at freeze-out. Generally, in a hot *r*-process, an extended $(n,\lambda) \rightleftarrows (\lambda,n)$ equilibrium is reached, and the location of the *r*-process path during the equilibrium phase is set by the nuclear masses for given values of neutron density and temperature of the astrophysical environment. So the *r*-process path is expected to be sensitive to the mass variations. In a cold *r*-process, the temperature and density drop quickly, so $(n,\lambda) \rightleftarrows (\lambda,n)$ equilibrium is established only briefly, which is quickly replaced by a new equilibrium between β decays and neutron captures. So the equilibrium path in the cold *r*-process refers to the *r*-process path at the time when (approximate) equilibrium is established between β decays and neutron captures. In this phase, β decays and neutron captures compete with each other, and the *r*-process path is expected to be sensitive to the change of neutron capture rates which depend on the nuclear mass. In summary, the masses of nuclei lying along the equilibrium *r*-process path are influential to the final abundance distribution. In the scenarios considered here, the equilibrium phases as discussed above are maintained at the *r*-process freeze-out, so the most impactful nuclei lie along the *r*-process path at freeze-out, as shown in region I.

However, in the cases of *hot2* and *cold* scenarios, the nuclei in region I have small values of sensitivity measure F, which means that the mass variations in this region have little or no effect on the final abundance distribution. We find that at the time of freeze-out, the mass changes of some nuclei in region I lead to great differences in the abundance pattern at this time, but the overall abundance in the rare-earth region is still small. Subsequently, a large number of fission fragments are deposited at the rare-earth peak region for *hot2* and *cold* scenarios, which weakens the previous difference of rare-earth abundance distribution caused by mass variation. That is, the effect of the mass variation in region I on abundances is masked by the distribution of fission fragments. So in this case, nuclei in region I generally have smaller F values. For *hot1* and *cold-sym* scenarios, without the contribution of fission fragments to rare-earth region, the difference in abundance at freeze-out due to mass changes in region I is fully propagated to the final rare-earth peak abundance.

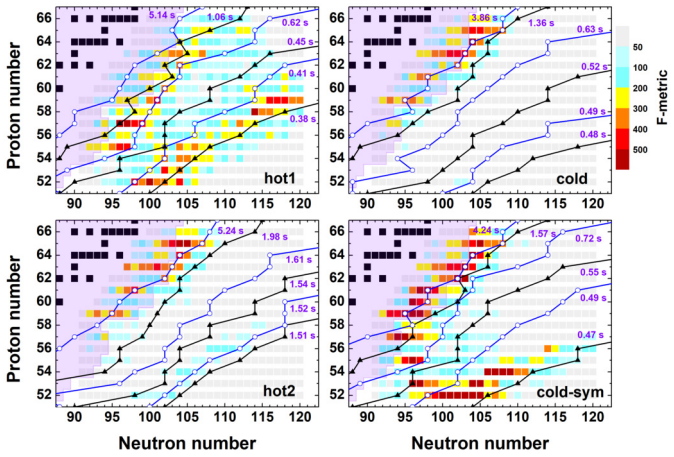

Fig. 3. Sensitivity measures F between ± 1 MeV mass variations in four different scenarios. The region of measured nuclear masses from AME2020 [58] is overlaid with pink color and black squares are stable isotopes. The black and blue lines represent the *r*-process paths at different times. The times of 0.38 s, 1.51 s, 0.48 s, and 0.47 s correspond to the *r*-process freeze-out, and the times of 0.62 s, 5.24 s, 3.86 s, and 4.24 s correspond to the point of $\tau_{n\gamma} \approx 3\tau_\beta$, in *hot1*, *hot2*, *cold*, and *cold-sym* scenarios, respectively.

The rare-earth peak is formed as the *r*-process path reach region II, and the shape of rare-earth peak is sensitive to the mass variation of the nuclei in this region. We find that the nuclei with high sensitivity measures F in region II lie along the *r*-process path at the time of $\tau_{n\gamma} \approx 3\tau_\beta$, corresponding to 0.62 s, 5.24 s, 3.86 s, and 4.24 s in *hot1*, *hot2*, *cold*, and *cold-sym* scenarios respectively as shown in Fig. 3. At this point, the rare-earth peak is successfully formed except the cold-sym case. When the *r*-process path continues to approach the β-stable line, β decay takes over completely and sensitivity measure F decreases.

In the cases of *hot2* and *cold* scenarios, the strong deposition of fission products erases the sensitivities to masses along the early *r*-process path (region I). However, the contribution of fission fragments to the rare-earth peak abundances decreases over time during the decay back to stability, because the fission flow gradually decreases at late time as shown in Ref. [46]. So as the *r*-process path moves toward stability, the contribution of fission fragments gradually decreases, and hence the weakening effect of fission fragments on the difference of abundance distribution caused by mass variation becomes weaker. Therefore, when the *r*-process path reaches region II, the sensitivities to nuclear masses are not easily concealed by the distribution of fission fragments, so nuclei in region II still have larger F values.

We highlight the effect of an individual mass change on the final abundances in Fig. 4. Nuclei with high sensitivity measure F from region I (if any) and region II were chosen from the *hot1*, *hot2*, *cold*, and *cold-sym* mass sensitivity studies of Fig. 3. Each nuclear mass has been changed by $\pm$ 1 MeV and the resultant final abundance pattern is compared to both the baseline and solar abundances. The figure shows that the single nuclear mass with high sensitivity measure has big influences on the rare-earth peak abundance distribution. We find that the variation of nuclear mass

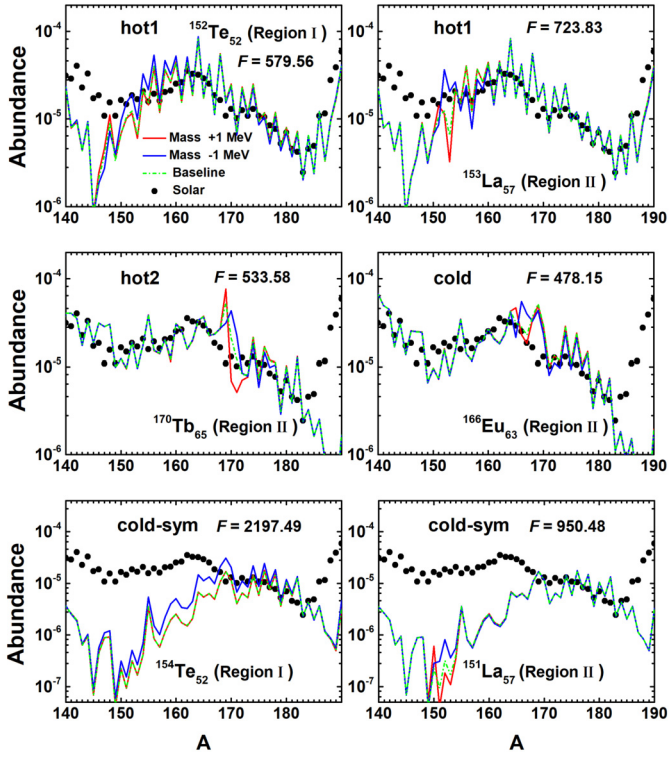

Fig. 4. The effect of mass variations on the final rare-earth peak abundances for selected nuclei in different scenarios. The baseline curve is represented by a dashed green line, and the red and blue lines represent the final abundances corresponding to the ± 1 MeV variation of nuclear masses. The dots represent the solar *r*-process abundance pattern.

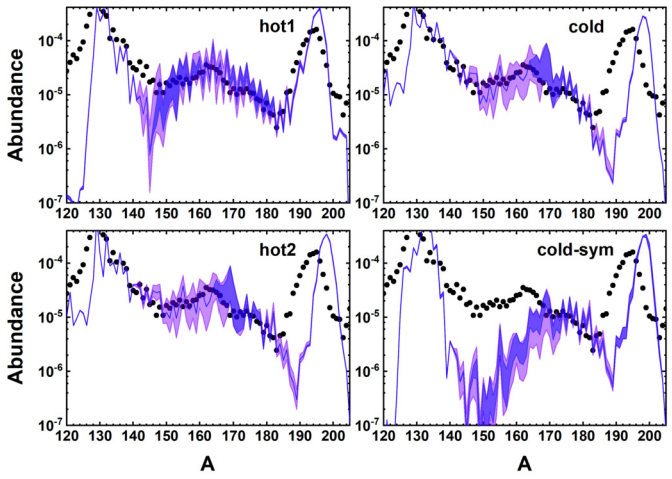

Fig. 5. Variances of the *r*-process abundances (shaded bands) corresponding to the sensitivity studies of ΔM = ±1 MeV for different scenarios. Darker shaded bands indicate the abundance variances caused by mass changes of 10 nuclei with the highest sensitivity measure *F* in the experimental unknown region. The masses are varied individually for each nucleus.

in region II, such as $^{153}La_{57}$, $^{170}Tb_{65}$, $^{166}Eu_{63}$, and $^{151}La_{57}$, affects the local structure of the rare-earth peak abundance distribution curve. In contrast, for $^{152}Te_{52}$ and $^{154}Te_{52}$ in region I further away from stability line, the influence on abundance can propagate to many other nuclei, affecting a larger mass range in rare-earth peak abundance distribution than the case of region II. It is also noticed that mass changes in the rare-earth region have no effect on the second and third *r*-process peaks.

In order to explore how much uncertainty in the final abundance pattern are produced due to the uncertainties in nuclear masses in the rare-earth region, we use our sensitivity study results to estimate the resulting error bars on the abundance pattern. In each astrophysical scenario, the sensitivity studies are carried out by varying every single nuclear mass with ΔM= ±1 MeV for 414 nuclei in the *r*-process simulations, and the resultant 828 *r*-process abundance patterns are obtained and they form a band as shown in Fig. 5, which is represented by a lighter shaded band. Note that the lighter shaded bands are not realistic uncertainties in final abundances, because the variation ΔM= ±1 MeV as error bar of experimentally-known masses is overestimated. Instead, to exclude the abundance uncertainties caused by variations of experimentally-known masses, the darker shaded bands indicate the uncertainty in final abundances caused by mass changes of 10 most influential nuclei in the experimental unknown region, which could already cover most of the lighter shaded bands in the *hot1* and *cold-sym* scenarios, and the large uncertainty is mainly concentrated around $A \sim 170$ in the *hot2* and *cold* scenarios. In principle, the formation of the rare-earth peak can be used to constrain the *r*-process site. However, a mass change of 1 MeV can produce significant effects on the abundance distribution in the rare-earth mass region as shown in Fig. 5. Nuclear mass uncertainties for these nuclei with high sensitivity measures must be reduced in order to obtain precise abundance pattern predictions, and to determine the favorable *r*-process astrophysical conditions. Efforts by both experimental and theoretical nuclear physics are necessary for an improved determination of nuclear masses of neutron-rich nuclei. It should be noticed that variance band here is caused by the variation of only a single nucleus in each *r*-process simulation, which is different from the conventional uncertainty estimation by variations of nuclear masses throughout the whole nuclear chart simultaneously in each *r*-process simulation as in Ref. [13], and hence the variance bands obtained here are much smaller than those in Ref. [13].

4. Conclusion

In summary, we have performed a sensitivity study of the *r*-process rare-earth peak abundances to individual nuclear masses in different astrophysical scenarios. Our results show that the main time of rare-earth peak formation is between *r*-process freeze-out and the point of $\tau_{n\gamma} \approx 3\tau_{\beta}$. The most impactful nuclei are mainly distributed in two regions in the nuclear chart: the region of 20-30 neutrons away from stability (defined as region I) and the region of 7-15 neutrons away from stability (defined as region II). Region I is the location of nuclear flow around *r*-process freeze-out, that is, the location of *r*-process path at the onset of the rare-earth peak formation. The mass variation in this region affects the final isotopic abundance distribution of several mass number ranges in the rare-earth peak region. The nuclei with high sensitivity measures *F* in region II lie along the *r*-process path at the point of $\tau_{n\gamma} \approx 3\tau_{\beta}$ when the rare-earth peak is formed. The mass variation in this region affects the local structure of the rare-earth peak abundance distribution curve.

In the astrophysical scenarios where a large number of fission events occur, such as the cases of *hot2* and *cold*, the sensitivity to the nuclei in region I is washed out by a large number of fission fragments deposited at the rare-earth mass region. Accordingly, when symmetric fission fragment distribution is used, as in the case of *cold-sym*, the sensitivity of region I is increased again because the fission fragments do not contribute to the rare-earth mass region. However, the solar rare-earth peak abundance cannot be reproduced by using the symmetric fission treatment. Our results also show that in the astrophysical scenarios with fission involved, where a large number of fission products are deposited at the rare-earth mass region, the rare-earth peak abundances are

largely set by the distribution of fission fragments, although the dynamical mechanism also plays an important role.

The most impactful nuclei for different r-process scenarios provide recommended targets for future experimental and theoretical studies, some of which are within current or near-future experimental reach. It will increase our understanding for the formation mechanism of rare-earth peak as well as the efficacy of using the rare-earth peak to constrain the r-process astrophysical site. However, this sensitivity study does not include the impact of the β decay as nuclear mass is changed, which may affect the uncertainties in the rare-earth peak abundances. These additional uncertainties will be explored in the future work.

Declaration of competing interest

The authors declare that they have no known competing financial interests or personal relationships that could have appeared to influence the work reported in this paper.

Data availability

Data will be made available on request.

Acknowledgement

We acknowledge helpful discussions with Dr. F. Q. Chen and W. L. Lv. This work was supported by the "Young Scientist Scheme" of National Key Research and Development Program under grant No. 2021YFA1601500, the National Natural Science Foundation of China under grant Nos. 12075104, 11875070 and 11935001, and the Anhui project (Z010118169).

Appendix A

Table 1
The 30 most important nuclei from sensitivity studies for *hot1*, *hot2*, and *cold* astrophysical conditions. Asterisk denotes nucleus with experimental mass data in AME2020 mass table [58]. Since the solar rare-earth peak cannot be reproduced in *cold-sym* scenario, the corresponding sensitivity results are not shown here.

Hot1			Hot2			Cold		
Z	A	F	Z	A	F	Z	A	F
57	153	723.83	65	170	533.58	64	168	516.62
57	154	672.95	65	169	516.51	63	166	478.15
52	152	579.56	64	168	492.66	65	170	455.20
58	172	506.56	63	164	489.26*	65	169	445.92
59	175	499.88	65	168	410.70*	63	164	422.71*
57	156	469.78	61	159	408.72*	63	165	411.81*
52	156	462.18	63	165	397.47*	61	159	377.66*
55	152	461.78	63	166	396.86	61	158	375.98*
59	177	456.09	61	158	383.38*	63	167	374.19
52	150	449.37	64	169	377.47	64	169	363.95
57	155	441.00	63	163	369.16*	62	164	351.91*
59	176	425.68	63	160	365.32*	59	155	351.78*
53	155	424.38	63	162	357.66*	65	168	350.08*
55	151	417.86	65	167	348.31*	65	172	345.09
59	160	406.14	62	164	335.74*	65	171	341.14
58	173	392.44	59	155	324.36*	63	163	333.29*
52	154	390.57	59	154	318.06*	59	154	324.27*
59	159	388.53	59	152	310.31*	65	173	312.94
54	158	379.61	65	171	309.74	63	162	309.69*
58	174	373.81	63	167	308.14	59	152	307.95*
55	159	369.46	65	172	301.70	59	156	294.16*
54	156	368.64	59	153	296.50*	59	153	290.77*
63	167	365.20	65	173	292.48	65	167	284.62*
57	169	364.57	65	166	288.66*	66	170	279.74
62	166	361.59	61	157	282.89*	57	151	278.35*
55	150	350.84	63	161	281.38*	61	157	268.83*
59	179	350.77	59	156	277.90*	61	160	254.76*
54	159	334.19	64	165	267.20*	66	171	249.68
55	161	323.57	66	170	260.05	64	165	248.62*
52	153	318.11	62	165	241.70	63	160	243.95*

References

[1] E.M. Burbidge, G.R. Burbidge, W.A. Fowler, F. Hoyle, Synthesis of the elements in stars, Rev. Mod. Phys. 29 (1957) 547–650, https://doi.org/10.1103/RevModPhys.29.547, https://link.aps.org/doi/10.1103/RevModPhys.29.547.

[2] Y.-Z. Qian, S.E. Woosley, Nucleosynthesis in neutrino-driven winds. I. The physical conditions, Astrophys. J. 471 (1) (1996) 331–351, https://doi.org/10.1086/177973.

[3] S. Wanajo, T. Kajino, G.J. Mathews, K. Otsuki, The r-process in neutrino-driven winds from nascent, "compact" neutron stars of core-collapse supernovae, Astrophys. J. 554 (1) (2001) 578–586, https://doi.org/10.1086/321339.

[4] C. Winteler, R. Käppeli, A. Perego, A. Arcones, N. Vasset, N. Nishimura, M. Liebendörfer, F.K. Thielemann, Astrophys. J. Lett. 750 (1) (2012) L22, https://doi.org/10.1088/2041-8205/750/1/L22, arXiv:1203.0616.

[5] S. Wanajo, Y. Sekiguchi, N. Nishimura, K. Kiuchi, K. Kyutoku, M. Shibata, Production of all the r-process nuclides in the dynamical ejecta of neutron star mergers, Astrophys. J. Lett. 789 (2) (2014) L39, https://doi.org/10.1088/2041-8205/789/2/L39, arXiv:1402.7317.

[6] K. Hotokezaka, P. Beniamini, T. Piran, Neutron star mergers as sites of r-process nucleosynthesis and short gamma-ray bursts, Int. J. Mod. Phys. D 27 (13) (2018) 1842005, https://doi.org/10.1142/S0218271818420051.

[7] T. Kajino, W. Aoki, A. Balantekin, R. Diehl, M. Famiano, G. Mathews, Current status of r-process nucleosynthesis, Prog. Part. Nucl. Phys. 107 (2019) 109–166, https://doi.org/10.1016/j.ppnp.2019.02.008, https://www.sciencedirect.com/science/article/pii/S0146641019300201.

[8] J.J. Cowan, C. Sneden, J.E. Lawler, A. Aprahamian, M. Wiescher, K. Langanke, G. Martínez-Pinedo, F.-K. Thielemann, Origin of the heaviest elements: the rapid neutron-capture process, Rev. Mod. Phys. 93 (2021) 015002, https://doi.org/10.1103/RevModPhys.93.015002, https://link.aps.org/doi/10.1103/RevModPhys.93.015002.

[9] B. Wehmeyer, M. Pignatari, F.-K. Thielemann, Galactic evolution of rapid neutron capture process abundances: the inhomogeneous approach, Mon. Not. R. Astron. Soc. 452 (2) (2015) 1970–1981, https://doi.org/10.1093/mnras/stv1352, https://academic.oup.com/mnras/article-pdf/452/2/1970/18504784/stv1352.pdf.

[10] S. Shibagaki, T. Kajino, G.J. Mathews, S. Chiba, S. Nishimura, G. Lorusso, Relative contributions of the weak, main, and fission-recycling r-process, Astrophys. J. 816 (2) (2016) 79, https://doi.org/10.3847/0004-637X/816/2/79, https://dx.doi.org/10.3847/0004-637X/816/2/79.

[11] Y. Yamazaki, Z. He, T. Kajino, G.J. Mathews, M.A. Famiano, X. Tang, J. Shi, Possibility to identify the contributions from collapsars, supernovae, and neutron star mergers from the evolution of the r-process mass abundance distribution, Astrophys. J. 933 (1) (2022) 112, https://doi.org/10.3847/1538-4357/ac721c, https://dx.doi.org/10.3847/1538-4357/ac721c.

[12] D. Martin, A. Arcones, W. Nazarewicz, E. Olsen, Impact of nuclear mass uncertainties on the r process, Phys. Rev. Lett. 116 (2016) 121101, https://doi.org/10.1103/PhysRevLett.116.121101, https://link.aps.org/doi/10.1103/PhysRevLett.116.121101.

[13] M. Mumpower, R. Surman, G. McLaughlin, A. Aprahamian, The impact of individual nuclear properties on r-process nucleosynthesis, Prog. Part. Nucl. Phys. 86 (2016) 86–126, https://doi.org/10.1016/j.ppnp.2015.09.001, https://www.sciencedirect.com/science/article/pii/S0146641015000897.

[14] Z. Li, Z.M. Niu, B.H. Sun, Influence of nuclear physics inputs and astrophysical conditions on r-process, Sci. China, Phys. Mech. Astron. 62 (8) (2019) 982011, https://doi.org/10.1007/s11433-018-9355-y.

[15] T.M. Sprouse, R. Navarro Perez, R. Surman, M.R. Mumpower, G.C. McLaughlin, N. Schunck, Propagation of statistical uncertainties of Skyrme mass models to simulations of r-process nucleosynthesis, Phys. Rev. C 101 (2020) 055803, https://doi.org/10.1103/PhysRevC.101.055803, https://link.aps.org/doi/10.1103/PhysRevC.101.055803.

[16] X.D. Xu, B. Sun, Z.M. Niu, Z. Li, Y.-Z. Qian, J. Meng, Reexamining the temperature and neutron density conditions for r-process nucleosynthesis with augmented nuclear mass models, Phys. Rev. C 87 (2013) 015805, https://doi.org/10.1103/PhysRevC.87.015805, https://link.aps.org/doi/10.1103/PhysRevC.87.015805.

[17] A. Arcones, G.F. Bertsch, Nuclear correlations and the r process, Phys. Rev. Lett. 108 (15) (2012) 151101, https://doi.org/10.1103/PhysRevLett.108.151101, arXiv:1111.4923.

[18] R. Surman, J. Engel, J.R. Bennett, B.S. Meyer, Source of the rare-Earth element peak in r-process nucleosynthesis, Phys. Rev. Lett. 79 (1997) 1809–1812, https://doi.org/10.1103/PhysRevLett.79.1809, https://link.aps.org/doi/10.1103/PhysRevLett.79.1809.

[19] R. Orford, N. Vassh, J.A. Clark, G.C. McLaughlin, M.R. Mumpower, G. Savard, R. Surman, A. Aprahamian, F. Buchinger, M.T. Burkey, D.A. Gorelov, T.Y. Hirsh, J.W. Klimes, G.E. Morgan, A. Nystrom, K.S. Sharma, Precision mass measurements of neutron-rich neodymium and samarium isotopes and their role in understanding rare-Earth peak formation, Phys. Rev. Lett. 120 (2018) 262702, https://doi.org/10.1103/PhysRevLett.120.262702, https://link.aps.org/doi/10.1103/PhysRevLett.120.262702.

[20] M.R. Mumpower, G.C. McLaughlin, R. Surman, Formation of the rare-Earth peak: gaining insight into late-time r-process dynamics, Phys. Rev. C 85

(2012) 045801, https://doi.org/10.1103/PhysRevC.85.045801, https://link.aps.org/doi/10.1103/PhysRevC.85.045801.
[21] J. Wu, S. Nishimura, G. Lorusso, P. Möller, E. Ideguchi, P.-H. Regan, G.S. Simpson, P.-A. Söderström, P.M. Walker, H. Watanabe, Z.Y. Xu, H. Baba, F. Browne, R. Daido, P. Doornenbal, Y.F. Fang, N. Fukuda, G. Gey, T. Isobe, Z. Korkulu, P.S. Lee, J.J. Liu, Z. Li, Z. Patel, V. Phong, S. Rice, H. Sakurai, L. Sinclair, T. Sumikama, M. Tanaka, A. Yagi, Y.L. Ye, R. Yokoyama, G.X. Zhang, D.S. Ahn, T. Alharbi, N. Aoi, F.L. Bello Garrote, G. Benzoni, A.M. Bruce, R.J. Carroll, K.Y. Chae, Z. Dombradi, A. Estrade, A. Gottardo, C.J. Griffin, N. Inabe, D. Kameda, H. Kanaoka, I. Kojouharov, F.G. Kondev, T. Kubo, S. Kubono, N. Kurz, I. Kuti, S. Lalkovski, G.J. Lane, E.J. Lee, T. Lokotko, G. Lotay, C.-B. Moon, D. Murai, H. Nishibata, I. Nishizuka, C.R. Nita, A. Odahara, Z. Podolyák, O.J. Roberts, H. Schaffner, C. Shand, Y. Shimizu, H. Suzuki, H. Takeda, J. Taprogge, S. Terashima, Z. Vajta, S. Yoshida, 94 β-decay half-lives of neutron-rich _55Cs to _67Ho: experimental feedback and evaluation of the r-process rare-Earth peak formation, Phys. Rev. Lett. 118 (2017) 072701, https://doi.org/10.1103/PhysRevLett.118.072701, https://link.aps.org/doi/10.1103/PhysRevLett.118.072701.
[22] M. Vilen, J.M. Kelly, A. Kankainen, M. Brodeur, A. Aprahamian, L. Canete, T. Eronen, A. Jokinen, T. Kuta, I.D. Moore, M.R. Mumpower, D.A. Nesterenko, H. Penttilä, I. Pohjalainen, W.S. Porter, S. Rinta-Antila, R. Surman, A. Voss, J. Äystö, Precision mass measurements on neutron-rich rare-Earth isotopes at JYFLTRAP: reduced neutron pairing and implications for r-process calculations, Phys. Rev. Lett. 120 (2018) 262701, https://doi.org/10.1103/PhysRevLett.120.262701, https://link.aps.org/doi/10.1103/PhysRevLett.120.262701.
[23] R. Orford, N. Vassh, J.A. Clark, G.C. McLaughlin, M.R. Mumpower, D. Ray, G. Savard, R. Surman, F. Buchinger, D.P. Burdette, M.T. Burkey, D.A. Gorelov, J.W. Klimes, W.S. Porter, K.S. Sharma, A.A. Valverde, L. Varriano, X.L. Yan, Searching for the origin of the rare-Earth peak with precision mass measurements across Ce–Eu isotopic chains, Phys. Rev. C 105 (2022) L052802, https://doi.org/10.1103/PhysRevC.105.L052802, https://link.aps.org/doi/10.1103/PhysRevC.105.L052802.
[24] M. Vilen, J.M. Kelly, A. Kankainen, M. Brodeur, A. Aprahamian, L. Canete, R.P. de Groote, A. de Roubin, T. Eronen, A. Jokinen, I.D. Moore, M.R. Mumpower, D.A. Nesterenko, J. O'Brien, A.P. Perdomo, H. Penttilä, M. Reponen, S. Rinta-Antila, R. Surman, Exploring the mass surface near the rare-Earth abundance peak via precision mass measurements at JYFLTRAP, Phys. Rev. C 101 (2020) 034312, https://doi.org/10.1103/PhysRevC.101.034312, https://link.aps.org/doi/10.1103/PhysRevC.101.034312.
[25] M.R. Mumpower, G.C. McLaughlin, R. Surman, A.W. Steiner, The link between rare-Earth peak formation and the astrophysical site of the r process, Astrophys. J. 833 (2) (2016) 282, https://doi.org/10.3847/1538-4357/833/2/282, https://dx.doi.org/10.3847/1538-4357/833/2/282.
[26] M.R. Mumpower, G.C. McLaughlin, R. Surman, A.W. Steiner, Reverse engineering nuclear properties from rare Earth abundances in the r process, J. Phys. G, Nucl. Part. Phys. 44 (3) (2017) 034003, https://doi.org/10.1088/1361-6471/44/3/034003, https://dx.doi.org/10.1088/1361-6471/44/3/034003.
[27] N. Vassh, G.C. McLaughlin, M.R. Mumpower, R. Surman, Markov chain Monte Carlo predictions of neutron-rich lanthanide properties as a probe of r-process dynamics, Astrophys. J. 907 (2) (2021) 98, https://doi.org/10.3847/1538-4357/abd035.
[28] D.N. Schramm, W.A. Fowler, Synthesis of superheavy elements in the r-process, Nature 231 (1971) 103, https://doi.org/10.1038/231103a0.
[29] S. Goriely, J.-L. Sida, J.-F. Lemaître, S. Panebianco, N. Dubray, S. Hilaire, A. Bauswein, H.-T. Janka, New fission fragment distributions and r-process origin of the rare-Earth elements, Phys. Rev. Lett. 111 (2013) 242502, https://doi.org/10.1103/PhysRevLett.111.242502, https://link.aps.org/doi/10.1103/PhysRevLett.111.242502.
[30] M.R. Mumpower, G.C. McLaughlin, R. Surman, The rare Earth peak: an overlooked r-process diagnostic, Astrophys. J. 752 (2) (2012) 117, https://doi.org/10.1088/0004-637X/752/2/117, https://dx.doi.org/10.1088/0004-637X/752/2/117.
[31] A. Arcones, G. Martínez-Pinedo, Dynamical r-process studies within the neutrino-driven wind scenario and its sensitivity to the nuclear physics input, Phys. Rev. C 83 (2011) 045809, https://doi.org/10.1103/PhysRevC.83.045809, https://link.aps.org/doi/10.1103/PhysRevC.83.045809.
[32] M. Mumpower, R. Surman, D.L. Fang, M. Beard, A. Aprahamian, The impact of uncertain nuclear masses near closed shells on the r-process abundance pattern, J. Phys. G, Nucl. Part. Phys. 42 (3) (2015) 034027, https://doi.org/10.1088/0954-3899/42/3/034027, https://dx.doi.org/10.1088/0954-3899/42/3/034027.
[33] M.R. Mumpower, R. Surman, D.-L. Fang, M. Beard, P. Möller, T. Kawano, A. Aprahamian, Impact of individual nuclear masses on r-process abundances, Phys. Rev. C 92 (2015) 035807, https://doi.org/10.1103/PhysRevC.92.035807, https://link.aps.org/doi/10.1103/PhysRevC.92.035807.
[34] X.F. Jiang, X.H. Wu, P.W. Zhao, Sensitivity study of r-process abundances to nuclear masses, Astrophys. J. 915 (1) (2021) 29, https://doi.org/10.3847/1538-4357/ac042f, https://dx.doi.org/10.3847/1538-4357/ac042f.
[35] S. Brett, I. Bentley, N. Paul, R. Surman, A. Aprahamian, Eur. Phys. J. A 48 (2012) 184, https://doi.org/10.1140/epja/i2012-12184-4.
[36] A. Aprahamian, I. Bentley, M. Mumpower, R. Surman, Sensitivity studies for the main r process: nuclear masses, AIP Adv. 4 (4) (2014) 041101, https://doi.org/10.1063/1.4867193.
[37] J. Beun, J.C. Blackmon, W.R. Hix, G.C. McLaughlin, M.S. Smith, R. Surman, Neutron capture on 130sn during r-process freeze-out, J. Phys. G, Nucl. Part. Phys. 36 (2) (2008) 025201, https://doi.org/10.1088/0954-3899/36/2/025201.
[38] R. Surman, J. Beun, G.C. McLaughlin, W.R. Hix, Neutron capture rates near $a =$ 130 that effect a global change to the r-process abundance distribution, Phys. Rev. C 79 (2009) 045809, https://doi.org/10.1103/PhysRevC.79.045809, https://link.aps.org/doi/10.1103/PhysRevC.79.045809.
[39] M.R. Mumpower, G.C. McLaughlin, R. Surman, Influence of neutron capture rates in the rare Earth region on the r-process abundance pattern, Phys. Rev. C 86 (2012) 035803, https://doi.org/10.1103/PhysRevC.86.035803, https://link.aps.org/doi/10.1103/PhysRevC.86.035803.
[40] R. Surman, M. Mumpower, J. Cass, I. Bentley, A. Aprahamian, G.C. McLaughlin, Sensitivity studies for r-process nucleosynthesis in three astrophysical scenarios, EPJ Web Conf. 66 (2014) 07024, https://doi.org/10.1051/epjconf/20146607024.
[41] M. Mumpower, J. Cass, G. Passucci, R. Surman, A. Aprahamian, AIP Adv. 4 (2014) 041009, https://doi.org/10.1063/1.4867192.
[42] https://sourceforge.net/projects/nucnet-tools/.
[43] P. Moller, J. Nix, W. Myers, W. Swiatecki, Nuclear ground-state masses and deformations, At. Data Nucl. Data Tables 59 (2) (1995) 185–381, https://doi.org/10.1006/adnd.1995.1002, https://www.sciencedirect.com/science/article/pii/S0092640X85710029.
[44] https://tendl.web.psi.ch/tendl_2019/talys.html [link].
[45] https://reaclib.jinaweb.org/.
[46] Y.W. Hao, Y.F. Niu, Z.M. Niu, Influence of spontaneous fission rates on the r-process nucleosynthesis, Astrophys. J. 933 (1) (2022) 3, https://doi.org/10.3847/1538-4357/ac6fdc, https://dx.doi.org/10.3847/1538-4357/ac6fdc.
[47] B.S. Meyer, r-process nucleosynthesis without excess neutrons, Phys. Rev. Lett. 89 (2002) 231101, https://doi.org/10.1103/PhysRevLett.89.231101, https://link.aps.org/doi/10.1103/PhysRevLett.89.231101.
[48] B.S. Meyer, J.S. Brown, Survey of r-process models, Astrophys. J. Suppl. Ser. 112 (1) (1997) 199, https://doi.org/10.1086/313032, https://dx.doi.org/10.1086/313032.
[49] I.V. Panov, H.T. Janka, On the dynamics of proto-neutron star winds and r-process nucleosynthesis, Astron. Astrophys. 494 (3) (2009) 829–844, https://doi.org/10.1051/0004-6361:200810292, arXiv:0805.1848.
[50] S. Wanajo, Cold r-process in neutrino-driven winds, Astrophys. J. 666 (2) (2007) L77–L80, https://doi.org/10.1086/521724, arXiv:0706.4360.
[51] G. Martínez-Pinedo, T. Fischer, L. Huther, Supernova neutrinos and nucleosynthesis, J. Phys. G, Nucl. Part. Phys. 41 (4) (2014) 044008, https://doi.org/10.1088/0954-3899/41/4/044008, https://dx.doi.org/10.1088/0954-3899/41/4/044008.
[52] J. Chen, J.Y. Fang, Y.W. Hao, Z.M. Niu, Y.F. Niu, Impact of nuclear beta-decay half-life uncertainties on the r-process simulations, Astrophys. J. 943 (2) (2023) 102, https://doi.org/10.3847/1538-4357/acaeab, https://dx.doi.org/10.3847/1538-4357/acaeab.
[53] http://www.cenbg.in2p3.fr/GEF.
[54] N. Vassh, R. Vogt, R. Surman, J. Randrup, T.M. Sprouse, M.R. Mumpower, P. Jaffke, D. Shaw, E.M. Holmbeck, Y. Zhu, G.C. McLaughlin, Using excitation-energy dependent fission yields to identify key fissioning nuclei in r-process nucleosynthesis, J. Phys. G, Nucl. Part. Phys. 46 (6) (2019) 065202, https://doi.org/10.1088/1361-6471/ab0bea.
[55] C. Sneden, J.J. Cowan, R. Gallino, Neutron-capture elements in the early galaxy, Annu. Rev. Astron. Astrophys. 46 (1) (2008) 241–288, https://doi.org/10.1146/annurev.astro.46.060407.145207.
[56] M. Eichler, A. Arcones, A. Kelic, O. Korobkin, K. Langanke, T. Marketin, G. Martinez-Pinedo, I. Panov, T. Rauscher, S. Rosswog, C. Winteler, N.T. Zinner, F.-K. Thielemann, The role of fission in neutron star mergers and its impact on the r-process-process peaks, Astrophys. J. 808 (1) (2015) 30, https://doi.org/10.1088/0004-637x/808/1/30.
[57] S. Goriely, The fundamental role of fission during r-process nucleosynthesis in neutron star mergers, Eur. Phys. J. A 51 (2015) 22, https://doi.org/10.1140/epja/i2015-15022-3.
[58] M. Wang, W. Huang, F. Kondev, G. Audi, S. Naimi, The AME 2020 atomic mass evaluation (ii). Tables, graphs and references, Chin. Phys. C 45 (3) (2021) 030003, https://doi.org/10.1088/1674-1137/abddaf.